



A Material Removal Model for CMP Based on the Contact Mechanics of Pad, Abrasives, and Wafer

Dinçer Bozkaya^z and Sinan Müftü^z

Department of Mechanical Engineering, Northeastern University, Boston, Massachusetts 02115, USA

Applied pressure in chemical mechanical polishing (CMP) is shared by the two-body pad–wafer and the three-body pad–abrasive–wafer contacts. The fraction of applied pressure transferred through the particle contacts is a significant factor as most of the material removal is due to abrasive particles trapped in the pad–wafer interface. In this work, the contact of a rough, deformable pad and a smooth, rigid wafer with rigid particles in the contact interface is investigated by using contact mechanics and finite element modeling. The interactions between the pad, wafer, and abrasive particles are modeled at different scales of contact, starting from the particle–pad level and gradually expanding to the multiasperity contact of the pad and the wafer. Wear rate due to each abrasive particle is calculated based on the wafer–abrasive particle contact force and by considering adhesive and abrasive wear mechanisms. A thin passivated layer on the wafer surface is modeled to consider the effect of chemical reactions between slurry and wafer. Good agreement between the model and the experimental literature is found for the relationships between material removal rate and applied pressure, pad elastic modulus and porosity, particle size and concentration, and pad roughness and wafer hardness.

© 2009 The Electrochemical Society. [DOI: 10.1149/1.3231691] All rights reserved.

Manuscript submitted July 22, 2009; revised manuscript received August 24, 2009. Published October 7, 2009.

Chemical mechanical polishing (CMP) is a polishing method commonly used in the manufacturing of wafer-based integrated circuits (ICs). Since CMP was first introduced to the IC manufacturing in the mid-1980s by IBM, CMP became a key technology in generating planar surfaces for several semiconductor manufacturing processes.¹ CMP operation involves forcing a rotating wafer attached to a wafer carrier against a rotating polishing pad. The polishing pad is covered with liquid slurry, which contains abrasive particles. The chemical reactions between the CMP slurry and the wafer are the primary driver for preparing the surface for polishing. The chemical composition of the surface is modified by the chemically reactive slurry to favor higher wear rates. In addition to the chemical interactions, the pad–wafer interface experiences the effects of contact and lubrication. Three-body contact due to the abrasive particles caught between the pad and the wafer and two-body contact between the pad and the wafer provide the necessary physical force to remove the material from the wafer surface. While solid-body contact is taking place, the pad–wafer interface experiences the lubricating effect of the slurry flow.

The abrasive particles used in conventional polishing techniques are 2.5–3 times harder than the workpiece material. These techniques cause scratches and pitting on the surface and cracks in the subsurface of the workpiece. The passivation of the surface layer of the wafer (workpiece) is important to achieve smooth and planarized surfaces without any surface and subsurface defects.² For this reason, an effective CMP process should provide a balance between the chemical and mechanical effects. The Preston equation is widely used to calculate the material removal rate (MRR), which is given as follows³

$$RR = k_p P_o V_r \quad [1]$$

where RR is the removal rate with units of material depth/time, k_p is the Preston constant, P_o is the average push-down pressure, and V_r is the relative sliding velocity of the surfaces. The Preston equation indicates a linear variation in MRR with respect to applied pressure and relative velocity. There are various experimental studies indicating both linear and nonlinear applied pressure P_o relationships.^{4–10} Also, k_p is typically determined experimentally, and it conveniently includes the effects of other parameters that influence the outcome of polishing.

In this paper, we present a mechanistic model of the MRR in CMP. A hierarchical model of the particle–wafer–pad interactions, presented recently,¹¹ was combined with abrasive and adhesive wear models to obtain a wafer-level MRR model based on particle-level

interactions. The predictions of the model were compared with published experimental data. Material removal models were developed by considering a contact regime in the pad–wafer interface.^{2,12–14} The MRR model by Luo and Dornfeld¹² and by Qin et al.¹³ assumed a mixed contact regime, and the load on particles was found by using the real contact pressure at the pad–wafer interface. Particle and mixed contact regimes were formulated by Ahmadi and Xia¹⁴ for a hard pad/high particle concentration and soft pad/low particle concentration, respectively. Fu et al.² determined the partition of applied pressure to the pad–wafer direct contact and the pad–particle–wafer contact by assuming that the pad is a thin elastic beam supported by particles at the ends.

The model developed in this work uses contact mechanics and finite element (FE) modeling to enable the calculation of the load transferred by the particles onto the wafer as a function of typical CMP parameters. The influence of applied pressure, pad elastic modulus, pad porosity, pad topography, particle size and concentration, wafer hardness, and their interactions on the MRR is expressed in the following form

$$RR = k_w (E_s, E_p / E_p, \eta_w, \sigma_s, R_s, \sigma_p, H_{pw}, H_{bw}, t_{pw}) f(P_o) V_r \quad [2]$$

where E_s and E_p are the solid pad elastic modulus and the porous pad elastic modulus, respectively, η_w is the weight particle concentration of the slurry, σ_s is the standard deviation (SD) of pad-asperity summit heights, R_s is the mean radius of the pad asperities, σ_p is the SD of the particle size, H_{pw} and H_{bw} are the passivated and bulk wafer hardness values, respectively, and t_{pw} is the thickness of the passivated layer. The function f describes the variation in MRR with respect to the applied pressure P_o . The MRR is assumed to increase linearly with relative velocity V_r as the lubrication effects are neglected in this work. The flow of the slurry causes hydrodynamic lubrication in the pad–wafer interface and thus influences the force equilibrium between the pad and the wafer. High deformability of the polishing pad strongly influences the interfacial behavior, and the resulting effects have been called soft-elastohydrodynamic lubrication.^{15–19} In addition to influencing the macroscale force balance, the slurry lubrication can also influence the contact conditions in the asperity wafer interface.²⁰ These effects are not considered in this work.

The applied pressure on the wafer is carried in part by the two-body pad-to-wafer contact (direct contact) and in part by the three-body contact of the pad, the wafer, and the abrasive particles (particle contact). The fraction of the applied pressure carried by the particle contacts is an important factor affecting the MRR as the majority of the material is removed by the abrasive particles trapped between the pad asperities and the wafer. Therefore, the calculation

^z E-mail: bozkaya@coe.neu.edu; s.muftu@neu.edu

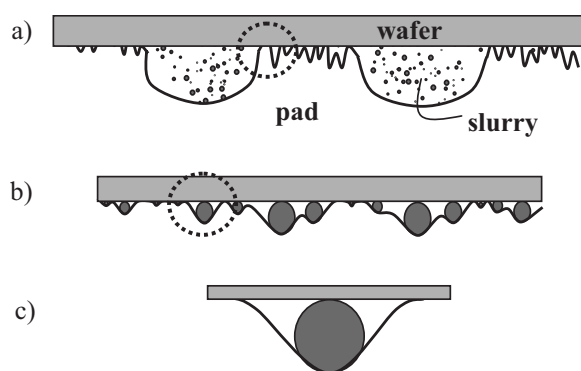


Figure 1. Different scales of contact.

of the applied pressure carried by particles is critical for the accuracy of the material removal models developed to predict MRR in CMP.

Modeling of Pad-Particle-Wafer Interactions

Different scales of contact encountered in CMP, as illustrated in Fig. 1a-c, were modeled starting from the smallest contact scale of a particle trapped between the pad and the wafer and gradually expanding to the pad-wafer rough contact, which is the largest contact scale considered in this work. Particle-level interactions were modeled in two steps, the single particle (SP) contact model and the

elastic modulus E_s . Therefore, the solid pad elastic modulus was used in the SP and MP contact models, while the porous pad elastic modulus E_p was considered in the MA contact model.

SP contact model.—The contact of a rigid spherical particle, with radius r_p , trapped between two flat surfaces (one rigid and one deformable), as shown in Fig. 2, was investigated using an axisymmetric FE model constructed in Ansys 9.0 (Canonsburg, PA). The details of the analysis were reported in Ref. 11. The two-parameter Mooney-Rivlin hyperelastic material model was used to simulate the material behavior of the pad. In this model, strain energy density function was expressed in terms of two material constants, a_{10} and a_{01} . Here, a_{10} and a_{01} were taken to be 0.5 MPa, which yielded $E_s = 6$ MPa.²³ Poisson's ratio of elastic surface, $\nu_s = 0.49$, which is typical of nearly incompressible rubberlike materials, was used in the model.

In the particle contact regime (Fig. 2a), $0 < \delta_p < 2r_p$, the following curve fit relationship was established for the particle contact force f_p^p ¹¹

$$f_p^p = \frac{E_s}{1 - \nu_s^2} r_p^2 \left[\frac{4}{3} \left(\frac{\delta_p}{r_p} \right)^{3/2} - 0.10 \left(\frac{\delta_p}{r_p} \right)^{2.89} \right] \quad \text{for } 0 < \delta_p < 2r_p \quad [3]$$

where δ_p is the displacement of the rigid particle (Fig. 2a). In the mixed contact regime (Fig. 2b), $\delta_p > 2r_p$, the particle contact force f_p^m was expressed as a function of the average compressive strain $\varepsilon_s = \delta_d/t_s$ ¹¹

$$f_p^m = \frac{E_s}{1 - \nu_s^2} r_p^2 \begin{cases} 5.4(\varepsilon_s)^{0.57} + 3.12 & \text{for } 0 < \varepsilon_s < 0.05 \\ 11.1(\varepsilon_s - 0.05)^{0.90} + 4.10 & \text{for } 0.05 < \varepsilon_s < 0.2 \\ 40.94(\varepsilon_s - 0.2)^2 + 13.14(\varepsilon_s - 0.2) + 6.11 & \text{for } 0.2 < \varepsilon_s < 0.45 \end{cases} \quad [4]$$

multiparticle (MP) contact model, as shown in Fig. 1c and b, respectively. In the SP contact model depicted in Fig. 2, the contact of an SP with one deformable surface (pad) and one rigid surface (wafer) was characterized using the FE method. Once the contact behavior of an SP was characterized, the overall effect of multiple particles on the contact of two flat surfaces (one rigid and one deformable) was modeled in the MP contact model (Fig. 1b). The results of the MP contact model were used in the multisasperity (MA) contact model to characterize the contact of a rough pad with a flat wafer surface in the presence of interfacial particles (Fig. 1a).

The elastic modulus of a porous pad E_p depends on the density ratio ρ_{po}/ρ_{so} and on whether or not the pad cells are open.²¹ E_p is one-fourth to one-third of the elastic modulus of the polymer substrate material E_s for typical pads.²² The pad porosity was introduced to the model by considering the relative size of the abrasives with respect to the pad asperity. We assumed that the pad's local interactions with the abrasives were dominated by the solid pad

where $\delta_d (= \delta_p - 2r_p)$ is the displacement of the deformable medium due to a direct contact and t_s is the thickness of the pad. In the mixed contact regime, the influence radius r_i and the pad-to-wafer direct contact pressure p_d^m , defined in Fig. 2b, were also required. The variation in these parameters were described using the following relationships¹¹

$$r_i = 1.52r_p(\varepsilon_s)^{-0.45} \quad \text{for } 0 < \varepsilon_s < 0.45 \quad [5]$$

$$p_d^m = \frac{E_s}{1 - \nu_s^2} \begin{cases} 0.76\varepsilon_s & \text{for } 0 < \varepsilon_s < 0.015 \\ 0.85(\varepsilon_s - 0.015) + 0.011 & \text{for } 0.015 < \varepsilon_s < 0.2 \\ 1.8(\varepsilon_s - 0.2)^{1.16} + 0.17 & \text{for } 0.2 < \varepsilon_s < 0.45 \end{cases} \quad [6]$$

MP contact model.—In the MP contact model, the local contact of two flat surfaces (one deformable and one rigid) was analyzed in the presence of rigid interfacial abrasive particles with different sizes. In the particle contact regime of the MP model, light external forces are transmitted between two surfaces by particle contacts alone; in the mixed contact regime, direct contact of the surfaces participates in load transmission with increasing external forces. These regimes are depicted schematically in Fig. 3. To calculate the particle and direct contact pressures, the outputs of the SP contact model were integrated over all active particles. The number of particles η_v per unit volume of the slurry can be found by the following relationship if we assume that the particles are spherical and that the probability density distribution of the particle size Φ_p and the weight particle concentration η_w are known

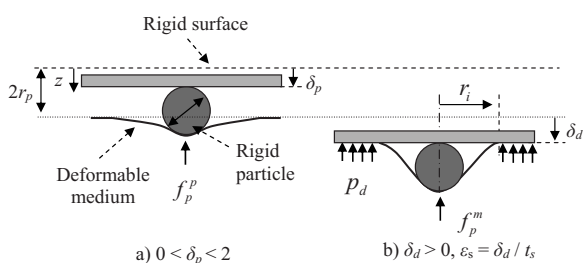


Figure 2. The SP contact model at different particle penetrations.

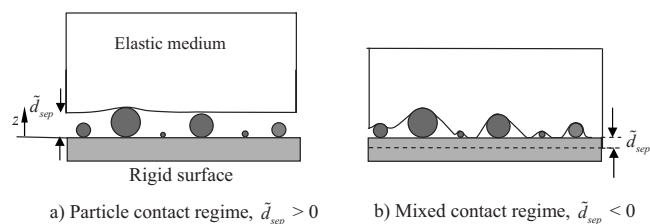


Figure 3. The MP contact model.

$$\eta_v = \frac{\rho_s}{\rho_p} \frac{\eta_w}{\int_0^\infty \frac{4}{3} \pi r_p^3 \Phi_p(r_p) dr_p} \quad [7]$$

where ρ_p and ρ_s are the mass densities of the particles and slurry, respectively.

When two rigid surfaces are separated by a distance d_{sep} , only the particles with diameters ($2r_p$) greater than this value are captured in the interface.¹³ Therefore, the number of active particles per unit contact area η_a^{mp} for a given separation distance is found by the summation of the number of particles with diameters greater than the separation distance as follows¹¹

$$\eta_a^{mp}(d_{sep}) = \eta_v \int_{d_{sep}/2}^\infty 2r_p \Phi_p(r_p) dr_p \quad [8]$$

The number of active particles in the mixed contact regime is found by setting $d_{sep} = 0$ in Eq. 8.

In the particle contact regime, $d_{sep} > 0$ (Fig. 3a), all the load is carried by particle contacts. The mean particle contact pressure p_p^{mp-p} can be found by using the number of the active particles η_a^{mp} from Eq. 8 and the load-displacement function f_p^p from Eq. 3, along with the relationship $\delta_p = (2r_p - d_{sep})$ as follows¹¹

$$p_p^{mp-p} = \frac{E_s}{1 - \nu_s^2} \eta_v \int_{d_{sep}/2}^\infty 2r_p f_p^p(\delta_p) \Phi_p(r_p) dr_p \quad \text{for } d_{sep} > 0 \quad [9]$$

In the mixed contact regime, $d_{sep} < 0$ (Fig. 3b), the total mean contact pressure p_c^{mp} has contributions due to the contact of the wafer with the particles (p_p^{mp-m}) and with the pad (p_d^{mp}), thus $p_c^{mp} = p_p^{mp-m} + p_d^{mp}$. The mean contact pressure p_p^{mp-m} due to particle contacts is found by using the average compressive strain $\varepsilon_p = d_{sep}/t_s$ in the load-displacement function f_p^m from Eq. 4 as follows

$$p_p^{mp-m} = \frac{E_s}{1 - \nu_s^2} \eta_v \int_0^\infty 2r_p f_p^m(-\varepsilon_p) \Phi_p(r_p) dr_p \quad \text{for } d_{sep} < 0 \quad [10]$$

The number of active particles η_a^{mp} from Eq. 8 remains constant in this regime.

The direct contact pressure p_d^{mp} requires knowledge of the direct contact area $A_d^{mp} = 1 - A_i$, where A_i is the total influence area. The total influence area of the particles as a fraction of the total area A_i can be found by the summation of the influence areas of individual particles πr_i^2 as follows

$$A_i^{mp} = \eta_v \int_0^\infty 2r_p \pi r_i^2 (-\varepsilon_p) \Phi_p(r_p) dr_p \quad [11]$$

where r_i is given by Eq. 5. The direct contact pressure p_d^{mp} can then be found by using the following relationship¹¹

$$p_d^{mp} = \frac{E_s}{1 - \nu_s^2} \int_{\varepsilon_p^m}^{\varepsilon_p} p_d^m(\varepsilon_p^r - \varepsilon_p) \frac{dA_d^{mp}}{d\varepsilon_p^r} d\varepsilon_p^r \quad [12]$$

Modeling of Material Removal

Next, wear rate relationships are introduced for a rigid spherical particle sliding with velocity V_r over a wafer and with hardness H_w under the influence of normal force f_w . Both adhesive and abrasive wear mechanisms are considered. In adhesive wear, the wear rate RR_{ad}^{sp} is calculated as follows²⁴

$$RR_{ad}^{sp} = \frac{k_w^{ad} V_r}{H_w} f_w \quad [13]$$

where k_w^{ad} is an empirically determined adhesive wear coefficient.

Abrasive wear occurs when the harder sphere digs into the softer substrate. The material is displaced from the groove in the form of loose wear particles.²⁴ The wear rate RR_{ab}^{sp} is proportional to the volume of the material swept by the abrasive particle. The instantaneous abraded area A_{ab}^{sp} caused by a rigid sphere sliding over a flat softer material can be found as follows²⁴

$$A_{ab}^{sp} = \sqrt{2} r_p \delta_w^{3/2} \quad [14]$$

by assuming that the indentation depth is small compared to a sphere radius $\delta_w \ll r_p$. If we assume that the load on the particle is sufficiently high to cause a fully plastic deformation in the softer material, the indentation depth can be calculated as follows²⁴

$$\delta_w = \frac{f_w}{H_w \pi r_p} \quad [15]$$

The total abrasive wear rate RR_{ab}^{sp} is proportional to the instantaneous abraded area A_{ab}^{sp} and the relative velocity V_r . An abrasive wear constant k_w^{ab} was used as only a fraction of the material was actually worn away from the groove. The abrasive wear relationship then becomes

$$RR_{ab}^{sp} = \left(\frac{k_w^{ab} V_r}{H_w^{3/2}} \right) \sqrt{\frac{2}{\pi^3}} \frac{f_w^{3/2}}{r_p} \quad [16]$$

Bilayer hardness model.— In CMP, material removal is achieved by a combination of mechanical and chemical effects. Chemicals in the slurry react with the wafer surface, forming a passivated layer and thus altering the hardness H_w of the wafer. The chemical reaction rates between the wafer material and slurry chemicals, the available reaction time, and the available amount of chemicals on the wafer surface affect the wafer hardness as a function of depth from the surface. A bilayer hardness model¹³ described by three parameters (the hardness H_{pw} and thickness t_{pw} of the passivated layer and the hardness H_{bw} of the bulk wafer) is adopted in this work to simplify hardness variation. This model assumes that the wafer hardness H_w is constant within the passivated layer, and the wafer material at a depth z larger than passivated layer thickness t_{pw} , $z > t_{pw}$, behaves as a bulk wafer material as follows

$$H_w(z) = \begin{cases} H_{pw} & z < t_{pw} \\ H_{bw} & z > t_{pw} \end{cases} \quad [17]$$

A sudden transition from H_{pw} to H_{bw} was assumed at $z = t_{pw}$. In reality, the hardness of the wafer is expected to vary more smoothly from the surface into the wafer.²⁵ The contact pressure acting at the wafer–particle interface is not uniform due to different hardness values of the passivated layer H_{pw} and bulk wafer H_{bw} . In this case, we assumed that the wafer–particle contact was sustained by the contributions from the contact pressure acting at the particle–passivated layer and particle–bulk wafer interfaces as follows

$$f_w = \frac{\pi}{2} [(a_w^2 - a_{bw}^2) H_{pw} + a_{bw}^2 H_{bw}] \quad \text{for } \delta_w > t_{pw} \quad [18]$$

where a_w and a_{bw} are the contact radii at the particle–passivated layer and particle–bulk wafer interfaces, respectively, as demonstrated in Fig. 4. The particle is considered to be sliding over the wafer; therefore, only half of the contact area is engaged in contact.

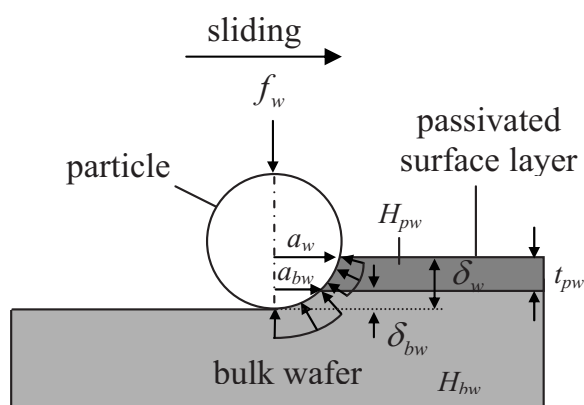


Figure 4. Bilayer hardness model.

By assuming that the indentation depths (δ_w and δ_{bw}) are small compared to the particle radius r_p , the contact radii (a_{pw} and a_{bw}) can be shown to be related to the indentation depth as follows

$$\delta_w = \frac{a_w^2}{2r_p} \quad \text{and} \quad \delta_{bw} = \frac{a_{bw}^2}{2r_p} \quad [19]$$

Using Eq. 18 and 19, the wafer-to-particle contact force f_w can be expressed in terms of indentation depth δ_w as

$$f_w = \pi r_p [(\delta_w - \delta_{bw})H_{pw} + \delta_{bw}H_{bw}] \quad [20]$$

Indentation depth δ_w is the summation of the thickness of the passivated layer, t_{pw} , and indentation depth in bulk wafer, $\delta_w = t_{pw} + \delta_{bw}$. Therefore, Eq. 20 reduces to

$$f_w = \pi r_p [t_{pw}H_{pw} + (\delta_w - t_{pw})H_{bw}] \quad [21]$$

Equation 21 can be rewritten as follows

$$f_w = \pi r_p \delta_w H_w^{\text{eff}}(\delta_w) \quad [22]$$

where the effective wafer hardness H_w^{eff} is defined as

$$H_w^{\text{eff}}(\delta_w) = \begin{cases} H_{pw} & \text{for } \delta_w \leq t_{pw} \\ \frac{t_{pw}}{\delta_w} H_{pw} + \left(1 - \frac{t_{pw}}{\delta_w}\right) H_{bw} & \text{for } \delta_w > t_{pw} \end{cases} \quad [23]$$

The effective hardness is dominated by bulk wafer hardness, $H_w^{\text{eff}} \rightarrow H_{bw}$, as the indentation depth becomes very large $\delta_w \rightarrow \infty$ and by the passivated wafer hardness, $H_w^{\text{eff}} = H_{pw}$, for a small indentation depth, $\delta_w < t_{pw}$. Equation 23 was used in the model to characterize the effect of the slurry chemicals on the MRR. In the rest of the paper, the superscript "eff" is omitted for simplicity. The effect of the relative sliding velocity V_r , which influences the oxidizer concentration available to the surface through mass transport^{26,27} and the MRR, is not included in the definition of the effective wafer hardness. If the process was not limited by mass transport and if the time constant of the chemical reactions on the surface was faster than that of CMP, then the effective hardness would nearly remain the same²⁵ and no speed effect would be expected.

RFF.— The wear rate formulas given in Eq. 13 and 16 show that adhesive wear is linearly proportional to the contact force $RR_{ad}^{\text{SP}} \propto f_w$, but the abrasive wear has the nonlinear relationship $RR_{ab}^{\text{SP}} \propto f_w^{3/2}$. This difference is later shown to have a critical effect on the outcomes of adhesive and abrasive wear of the wafer. To highlight this effect, we defined the following two removal force functions (RFFs) for adhesive R_{ad}^{SP} and abrasive R_{ab}^{SP} wear

$$R_{ad}^{\text{SP}} = f_w \quad \text{and} \quad R_{ab}^{\text{SP}} = \sqrt{\frac{2}{\pi^3}} \frac{f_w^{3/2}}{r_p} \quad [24]$$

respectively. The MRR for each wear regime can be calculated from Eq. 13 and 16 by knowing the value of R^{SP} .

The RFF for the MP contact model, R^{MP} , was calculated by integrating the RFF due to each particle, R^{SP} , over all particles active in contact in a form similar to Eq. 9 and 10 as follows

$$R^{\text{MP}} = \begin{cases} \eta_v \int_{d_{\text{sep}}/2}^{\infty} 2r_p R^{\text{SP}} \Phi_p(r_p) dr_p & \text{if } d_{\text{sep}} > 0 \\ \eta_v \int_0^{\infty} 2r_p R^{\text{SP}} \Phi_p(r_p) dr_p & \text{if } d_{\text{sep}} < 0 \end{cases} \quad [25]$$

From a practical point of view, it makes more sense to report the RFF as a function of the contact pressure p_c^{MP} acting between the two surfaces. To achieve this, the separation distance d_{sep} was used as an intermediate parameter, and the RFF was matched against the contact pressure p_c^{MP} through look-up tables by using Eq. 9, 10, 12, and 25.

MA contact between a rough pad and a wafer.— The contact between a rough pad and the wafer occurs at the tip of pad asperities. Let us first consider the contact of a pad single asperity with radius R_s and assume it to behave like a Hertz contact. Then, the mean contact pressure p_c^m and the contact radius a can be found from the following relationships²⁸

$$p_c^m = \frac{4E_p}{3\pi} \left(\frac{\delta_s}{R_s}\right)^{1/2} \quad \text{and} \quad a = (\delta_s R_s)^{1/2} \quad [26]$$

where E_p is the elastic modulus of the pad and δ_s is the pad-asperity deformation.

If we assumed that the presence of the abrasive particles in the asperity wafer interface did not influence the Hertz relationships (Eq. 26), then the mean contact pressure p_c^m could be used to find the RFF under each pad asperity. For a given asperity, once p_c^m was determined, the R^s per unit area can be found from the $R^{\text{MP}} - p_c^m$ relationship described above; R^s can be found from the following relationship

$$R^s = \pi a^2 R^{\text{MP}}(p_c^m) \quad [27]$$

The RFF due to the contact of a rough pad and a flat wafer with interfacial abrasive particles can then be computed by considering the following relationship

$$R = \eta_s \int_{d_{\text{wp}}}^{\infty} \pi a^2 R^{\text{MP}}(p_c^m) \Phi_s(z_s) dz_s \quad [28]$$

where η_s is the areal density of the pad-asperity summits, z_s is the peak height of the surface asperities, Φ_s is the probability density function (PDF) of asperity summit heights, and d_{wp} is the wafer to pad separation.

The applied pressure P_o is the controlled parameter in CMP, instead of the equilibrium separation distance d_{wp} , which can be obtained for a given d_{wp} as²⁹

$$P_o = \frac{4}{3} \eta_s E_p R_s^{1/2} \int_{d_{\text{wp}}}^{\infty} \Phi_s(z_s) (z_s - d_{\text{wp}})^{3/2} dz_s \quad [29]$$

Real contact area A_r and mean real contact pressure P_m ($P_m = P_o/A_r$) acting at the tip of asperities can be calculated from the following relationship²⁹

$$A_r = \pi \eta_s R_s \int_{d_{\text{sep}}}^{\infty} (z_s - d_{\text{sep}}) \Phi_s(z_s) dz_s \quad [30]$$

In the largest scale, the rough contact model, the direct contact area A_d , the particle contact pressure P_p , and the number of active par-

Table I. Physical values of parameters.

Parameter	Base	Range
SD of particle radius (σ_p)	6.25 nm	NA
Mean particle radius ($\mu_p = 4\sigma_p$)	25 nm	NA
Particle concentration (η_w)	2.5%	0–10%
Particle to slurry density ratio (ρ_p/ρ_s)	3.7 (alumina)	NA
Pad summit radius (R_s)	50 μm	25–100 μm
Pad summit density (η_s)	$2 \times 10^{-4}/\mu\text{m}^2$	NA
Pad summit SD (σ_s)	5 μm	1–20 μm
Solid pad elastic modulus (E_s)	10 (soft) and 100 (hard) MPa	10–100 MPa
Modulus ratio (E_s/E_p)	1 and 4	1–4
Applied pressure (P_o)	0.007 and 0.07 MPa (1 and 10 psi)	0–0.07 MPa (0–10 psi)

ticles n_a were calculated using relationships similar to Eq. 28 except that R^{mp} was replaced by the appropriate functions for A_d^{mp} , P_p^{mp} , and η_a^{mp} that are developed in the preceding sections.

Results and Discussion

In this paper, the effects of applied pressure, pad elastic properties, slurry particle concentration, pad topography, and wafer hardness on the MRR are presented. The base parameters used in the models and the range of values utilized to evaluate the effect of each parameter are listed in Table I.

Effect of applied pressure.—The effects of the applied pressure P_o and the pad elasticity on the RFF are presented for soft and hard pads ($E_s = 10, 100$ MPa) with different porosity levels ($1 \leq E_s/E_p \leq 4$), in Fig. 5. The characteristics of adhesive and abrasive wear models were found to be similar. Figure 5 represents the RFF due to adhesive wear R_{ad} . A sublinear variation in RFF is observed for a soft pad with high porosity (e.g., $E_s/E_p = 4$). The RFF increases almost linearly with applied pressure P_o for a hard pad or a nonporous pad ($E_s/E_p = 1$). The nonlinearity of the RFF with respect to the applied pressure P_o is quantified by applying a power law curve fit in the form $R = cP_o^n$. The power law exponent is found to be $n = 0.94$ for $E_s = 100$ MPa with $1 < E_s/E_p < 4$. In a soft pad ($E_s = 10$ MPa), the power law exponent decreases from $n = 0.94$ to 0.88 as the porosity is increased from $E_s/E_p = 1$ to 4. A similar behavior is observed for RFF due to abrasive wear.

These results can be explained by considering real contact area A_r and mean contact pressure P_m acting at the tip of the pad asperities in contact with a wafer. Real contact area A_r is the main controlling parameter for the number of active particles n_a . The mean real contact pressure P_m determines the local contact behavior affecting the distribution of contact pressure to particle and direct contacts. The mean real contact pressure P_m is found to remain

almost constant as the applied pressure P_o is increased. As a result, the direct contact area ratio A_d/A_r does not change significantly, as illustrated in Fig. 6a. Figure 6b shows that the number of active particles n_a increases with applied pressure as the real contact area becomes larger with higher applied pressure. Therefore, the sublinear variation seen in RFF for a soft pad is attributed to the sublinear increase in real contact area A_r and the number of active particles n_a . In this work, the asperity summit height distribution was taken to be Gaussian. The real contact area A_r increases linearly with applied pressure P_o if the tall asperities, which are in the upper part of the Gaussian distribution, are in contact.²⁹ This is the case for a hard pad, as illustrated in Fig. 7. The increase becomes sublinear when lower asperities start to come in contact for a soft pad, where the equilibrium separation distance is negative for the high applied pressure.

The experiments found in literature for the effect of applied pressure P_o were classified into two groups based on the pad elastic modulus E_s (hard or soft pads). The power law exponents of the P_o term of the MRR obtained from experiments^{4,10} are summarized in Table II. The power law exponent varies in the range of $0.84 < n < 1.04$ for hard pads, whereas it varies in the range of $0.53 < n < 0.89$ for soft pads. The tendency for the MRR to become sublinear with a softer pad agrees with modeling results. The models show a decrease in the power law exponent n from 0.93 to 0.88 as the pad elastic modulus is reduced from $E_s = 100$ MPa to $E_s = 10$ MPa, with $E_s/E_p = 4$. This result agrees with oxide CMP experiments, conducted by Hernandez et al.,⁶ indicating a decrease in power law exponent n from 0.96 to 0.89 when a soft pad is used instead of a hard pad. However, the power law exponent can be as small as $n = 0.53$ in the experiments, as shown in Table II, while modeling results using base parameters did not result in a power law exponent $n < 0.88$. This discrepancy could be explained by considering the assumption of using the Gaussian distribution for asperity summit

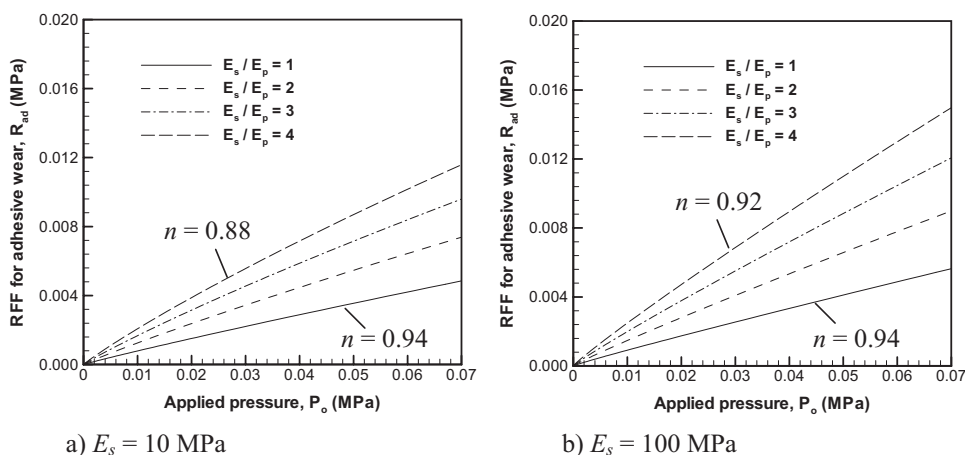


Figure 5. The variation in the RFF due to adhesive wear R_{ad} with applied pressure P_o for (a) soft ($E_s = 10$ MPa) and (b) hard ($E_s = 100$ MPa) pads with different porous elastic modulus ratios E_s/E_p .

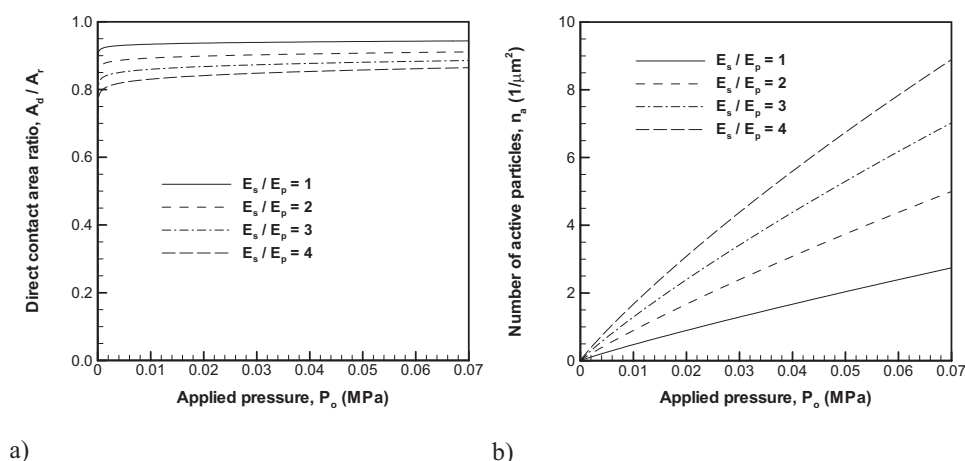


Figure 6. The variation in (a) direct contact area ratio A_d/A_r and (b) number of active particles n_a for a soft pad, $E_s = 10$ MPa, with different porous elastic modulus ratios E_s/E_p .

heights for the pad. A different assumption for pad topography causes the power law exponents to change. Ahmadi and Xia¹⁴ and Luo and Dornfeld¹² explained the sublinear behavior by considering a wavy pad topography, which gives a relation between applied pressure P_o and real contact area A_r as $P_o \propto A_r^{2/3}$. Using this relationship, our model for a soft pad would result in a power law exponent of $n \approx 2/3$ as the real contact area A_r is the main controlling parameter for the effect of applied pressure P_o .

Effect of pad elastic modulus and pad porosity.— Figure 8 shows the effect of pad elastic modulus E_s and pad porosity on the RFF for constant applied pressure, $P_o = 0.007$ MPa (1 psi). The behavior observed for the applied pressure in the range of $0.007 < P_o < 0.07$ MPa is similar; therefore, only the plots for P_o

$= 0.007$ MPa are included here. Figure 8a shows that the RFF increases slightly with the pad elastic modulus E_s for adhesive wear. An order of magnitude increase in the pad elastic modulus E_s from 10 to 100 MPa results in only $\sim 18\%$ higher RFF for adhesive wear R_{ad} . The pad elastic modulus causes a more significant effect for the RFF for abrasive wear R_{ab} , as shown in Fig. 8b. An ~ 3.7 -fold increase in R_{ab} can be observed when E_s is increased from 10 to 100 MPa.

As the pad porosity (E_s/E_p ratio) is increased, the RFF due to both adhesive and abrasive wear becomes larger, as illustrated in Fig. 8. Increasing the modulus ratio (E_s/E_p) from 1 to 4 causes the RFF due to adhesive R_{ad} and abrasive R_{ab} wear to increase to ~ 2.6 and ~ 2.3 times, respectively.

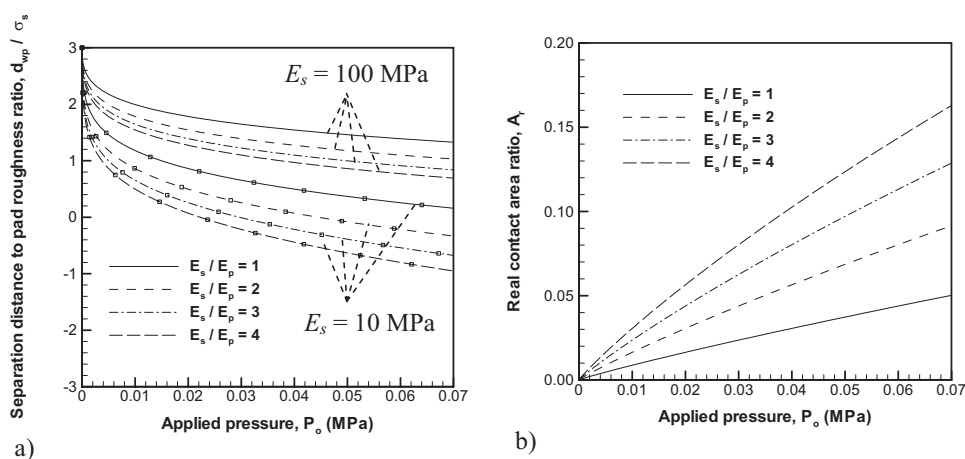


Figure 7. The equilibrium separation distance d_{wp}/σ_s as a function of applied pressure P_o for different pad elastic moduli E_s and porous elastic modulus ratios E_s/E_p .

Table II. Summary of power law exponents determined in experiments, organized to demonstrate the effect of pad elastic modulus.

Experiments	Polishing pad	Polished film	Slurry	Applied pressure (psi)	Power law exponent
Nguyen et al. ⁴	Hard	Copper	Alumina	2.8–4.9	0.99
Clark et al. ⁵	Hard	Oxide	Silica	2–8	¹²ⁿ¹ 1.04–0.84 ¹²ⁿ¹
Hernandez et al. ⁶	Hard	Oxide	Silica	2.8–5.8	0.96
Forsberg ⁷	Soft	Oxide	Silica	0.5–4.8	0.62
Chandrasekaran et al. ⁸	Soft	Tetraethyl orthosilicate	Silica	1–7	0.53
Guo and Subramanian ⁹	Soft	Copper	Alumina	0.3–13.3	0.54
Hernandez et al. ⁶	Soft	Oxide	Silica	2.8–5.8	0.89
Wrschka et al. ¹⁰	Soft	Aluminum	Alumina	2.8–5.8	0.80
Wrschka et al. ¹⁰	Soft	Aluminum	Silica	2.8–5.8	0.86

^a IC1400pad.

^b IC1000pad.

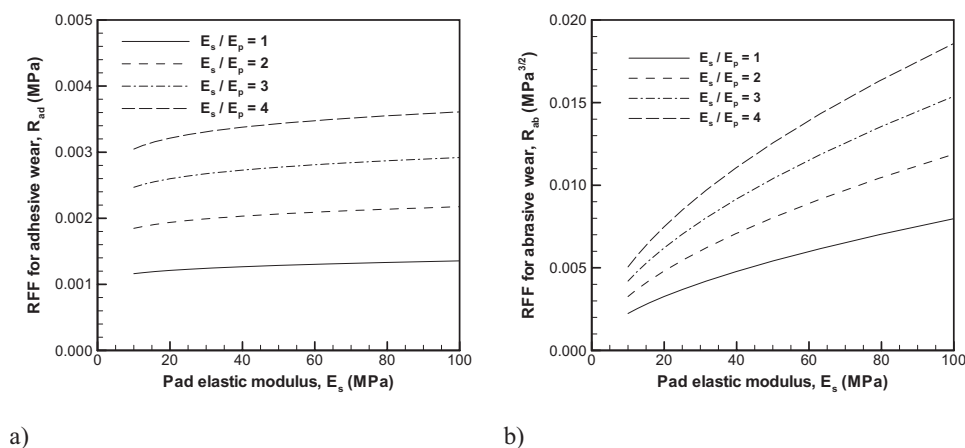


Figure 8. The effect of pad elastic modulus E_s on the RFF due to (a) adhesive wear R_{ad} and (b) abrasive wear R_{ab} for $P_o = 0.007$ MPa (or $P_o = 1$ psi).

These results are explained by considering the variation in direct contact area ratio A_d/A_r and mean particle contact force f_w^m , plotted in Fig. 9a and b, respectively. The elastic modulus of the solid pad material E_s affects the particle penetration in the pad–particle interface. For stiffer pads (large E_s), pad-to-wafer direct contact becomes more difficult, and the direct contact area ratio A_d/A_r becomes smaller. The porous elastic modulus of the pad E_p controls the local contact pressure acting at the pad-asperity tips. As the pad porosity increases (smaller E_p), the asperity contact spreads over a larger area; i.e., the real contact area A_r increases, thus causing a mean real contact pressure P_m at the tip of asperities (local contact pressure) to decrease. The lower mean real contact pressure P_m decreases the direct contact area A_d/A_r . If solid E_s and porous E_p pad elastic moduli increase or decrease at the same rate, such that the porous elastic modulus ratio E_s/E_p is constant, the direct contact area A_d/A_r and the RFF due to adhesive wear R_{ad} , as a result, do not change significantly because the effects of E_s and E_p on R_{ad} offset each other. In abrasive wear, although this effect is the same, higher mean particle contact force f_w^m causes the RFF for abrasive wear R_{ab} to increase as the pad elastic modulus E_s becomes larger.

Guo and Subramanian⁹ carried out copper CMP experiments with alumina slurry using the same conditions [$P_o = 0.47$ MPa (6.8 psi), $V_r = 0.47$ m/s, and $\eta_w = 2.5\%$] for a soft (Suba-500) and a hard (IC1000) pad. They found that the MRR for the hard and soft pads were ~ 245 and ~ 110 nm/min, respectively. The ratio of MRR for a hard to a soft pad was ~ 2.2 . The same ratio predicted for adhesive and abrasive wear using $E_s = 10$ MPa for a soft pad and $E_s = 100$ MPa for a hard pad with $E_s/E_p = 4$ was 1.2 and 3.7, respectively, indicating that the experimental trend can be explained by considering both adhesive and abrasive wear taking place simultaneously.

A similar experiment was carried out by Saxena et al.²⁶ for CMP of copper films with alumina slurry [$P_o = 0.028$ MPa (4 psi) and $\eta_w = 3\%$]. A soft PANW pad (Freudenberg Nonwovens) and a hard IC1400 were used in their study. The ratio of MRR achieved by a hard pad (165 nm/min) to a soft pad (140 nm/min) was found to be 1.18, which is very close to the ratio (~ 1.2) calculated by our model with adhesive wear.

Experiments³⁰⁻³² indicate a general trend of increasing MRR with higher porosity, in agreement with model results. In the CMP experiments by Fury and James,³² one porous pad with a relative density $\rho_{po}/\rho_{so} = 0.6$ (IC1000) and one solid pad $\rho_{po}/\rho_{so} = 1$ (IC2000) made from the same polyurethane material were used. Because the pads were made of the same polyurethane material, it can be assumed that the solid pad elastic modulus E_s is the same for these two pads, while the porous elastic modulus ratio E_s/E_p can be estimated to be $E_s/E_p \approx 3$ for $\rho_{po}/\rho_{so} = 0.6$.²¹ The pads were roughened by using the same conditioning parameters to ensure that the surface topography of the pads were similar. The average MRR for a porous pad (IC1000) was found to be $\sim 40\%$ higher than that of a solid pad (IC2000). This finding qualitatively agrees with the results of our model (Fig. 8), indicating an increasing trend for MRR with increasing pad porosity. Figure 10 shows the effects of pad porosity and slurry particle concentration on the ratio of RFF values for porous and nonporous pads with $E_s/E_p = 3$ and 1, respectively. The solid pad elastic modulus was $E_s = 100$ MPa, and the applied pressure was maintained at $P_o = 0.007$ MPa. Because the particle concentration η_w used in the experiments³² was not specified, the ratio of RFF for a porous and a nonporous pad was plotted as a function of particle (silica) concentration. RFF for a porous pad is greater

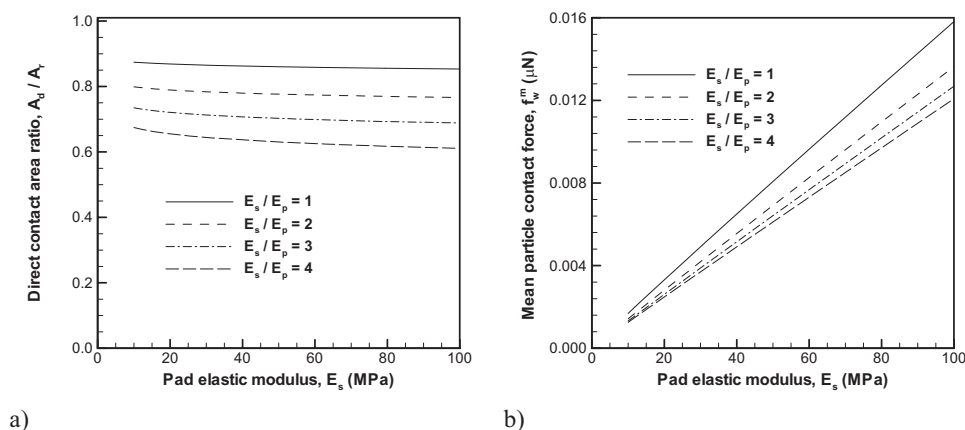


Figure 9. The effect of pad elastic modulus E_s on (a) direct contact area ratio A_d/A_r and (b) mean particle contact force f_w^m for $P_o = 0.007$ MPa (or $P_o = 1$ psi).

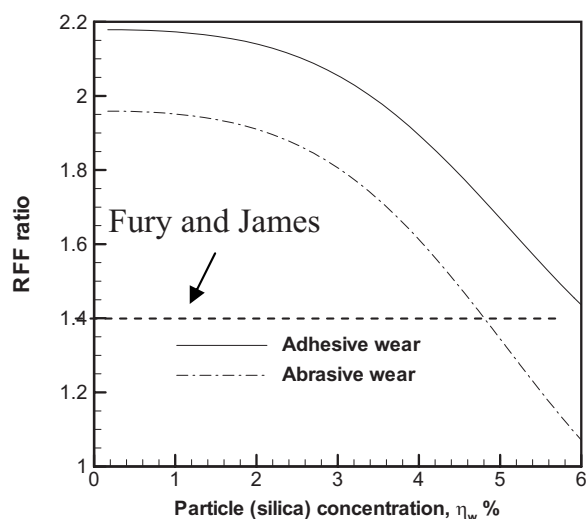


Figure 10. Model predictions for the ratio of RFF for a porous ($E_s/E_p = 3$) to RFF for a solid pad ($E_s/E_p = 1$) as a function of particle (silica) concentration η_w . The dotted line indicates the ratio determined in the experiments by Fury and James.³⁴

than a solid pad by 40% for adhesive wear at particle concentration, $\eta_w = 5\%$, and for abrasive wear at $\eta_w = 6\%$. The increase in MRR for larger porosity is predicted well by the model.

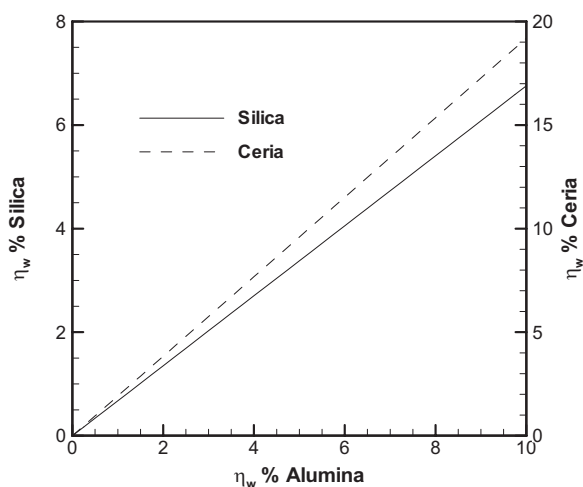


Figure 11. Equivalent particle concentration η_w by weight ratio of particles of different materials to result in the same volumetric particle concentration, η_v .

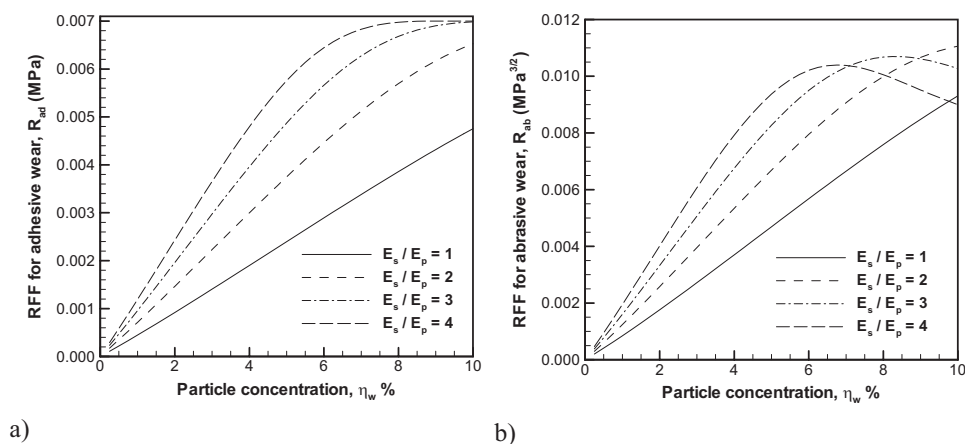


Figure 12. The effect of particle concentration η_w on RFF due to (a) adhesive wear R_{ad} and (b) abrasive wear R_{ab} for a low applied pressure $P_o = 0.007$ MPa (or $P_o = 1$ psi) and $E_s = 10$ MPa.

Effect of particle concentration.—In the models, volumetric particle concentration η_v is the main parameter controlling the number of particles entering the calculations. Particle concentration by weight ratio η_w is commonly used in practice because it is easier to measure for a slurry. For a given particle concentration η_w by weight ratio, volumetric particle concentration η_v can be calculated using the density of particle material, ρ_p , in Eq. 7. Although the modeling results are obtained for alumina particles ($\rho_{al} = 3.7$ g/cm³), results can be applied to different particle materials such as silica ($\rho_{si} = 2.5$ g/cm³) or ceria ($\rho_{ce} = 7.1$ g/cm³) by utilizing Fig. 11, which shows the equivalent particle concentration η_w by the weight ratio of different particle materials resulting in the same volumetric particle concentration η_v .

In Fig. 12a, RFF due to adhesive wear R_{ad} is plotted as a function of particle concentration, η_w for applied pressure, $P_o = 0.007$ MPa (or $P_o = 1$ psi), and pad elastic modulus $E_s = 10$ MPa. In this range, the RFF due to adhesive wear R_{ad} increases linearly with the particle concentration η_w for a nonporous pad ($E_s/E_p = 1$). As the pad porosity increases, the variation in RFF due to adhesive wear R_{ad} with particle concentration η_w becomes sublinear. RFF due to adhesive wear R_{ad} levels off when the particle concentration $\eta_w > 8\%$ for $E_s/E_p = 4$, which is called the saturation particle concentration, η_w^c . We also determined that the saturation particle concentration η_w^c decreases with a larger pad elastic modulus E_s or while a higher applied pressure P_o increases η_w^c .³³

Similar to the behavior of the adhesive wear function R_{ad} , the abrasive wear function R_{ab} also increases with increasing particle concentration η_w , as illustrated in Fig. 12b. However, in abrasive wear, we see that R_{ab} reaches a peak at a critical particle concentration $\eta_w = \eta_w^c$ and drops with increasing η_w . The reasons for the saturation in the adhesive and the peaking in the abrasive wear on the RFF with particle concentration η_w is explained next.

At a low particle concentration η_w , there are few active particles in the contact interface, and the mean spacing between particles is large, allowing direct contact to occur. As a result of the direct contact, a fraction of the applied pressure P_o is carried by direct contacts, and the particle contact pressure becomes $P_p/P_o < 1$. An increase in the particle concentration η_w results in an increase in the number of active particles n_a . This, in turn, causes the mean spacing between the particles to become smaller, reducing the direct contact area A_d . This effect is quantified in the results presented in Fig. 13a. As particle concentration reaches a critical value, $\eta_w = \eta_w^c$, the mean spacing between the particles becomes such that direct contact is prevented, and the applied pressure is transferred entirely through the particles. As a result, at the saturation particle concentration η_w^c , the direct contact becomes zero, $A_d = 0$, and the particle contact pressure becomes $P_p/P_o = 1$. Increasing particle concentration above this saturation value, $\eta_w > \eta_w^c$, does not change the fraction of the applied pressure P_o carried by particle contacts. Thus, we see

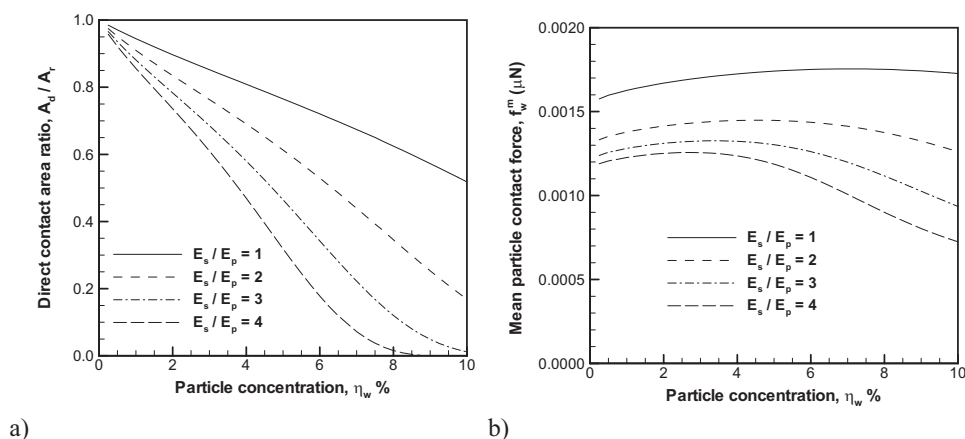


Figure 13. The effect of particle concentration η_w on (a) direct contact area ratio A_d/A_r and mean particle contact force f_w^m for $P_o = 0.007$ MPa (or $P_o = 1$ psi) and $E_s = 10$ MPa.

that the saturation particle concentration η_w^c is a critical factor in material removal. The magnitude of η_w^c increases using softer (small E_s) or lower porosity (small E_s/E_p) pads or by applying higher pressures P_o .

The behavior of adhesive (R_{ad}) and abrasive (R_{ab}) RFFs, when the particle concentration is greater than the saturation particle concentration, $\eta_w > \eta_w^c$, can be explained by considering the variation in the mean contact force f_w^m on each particle as a function of particle concentration, as shown in Fig. 13b. The mean particle contact force f_w^m is determined by the particle contact pressure P_p and the number of active particles n_a as $f_w^m = P_p/n_a$. Figure 13b shows that the mean particle contact force f_w^m decreases with increasing particle concentration, η_w , where the number of active particles n_a becomes larger. When $\eta_w > \eta_w^c$, the particle contact pressure, P_p remains constant. If the variation in RFF due to adhesive R_{ad} and abrasive R_{ab} wear achieved by all active particles is considered, $R_{ad} \propto n_a f_w^m$ and $R_{ab} \propto n_a f_w^{m3/2}$, the increase in the number of active particles n_a offsets the decrease in mean contact force f_w^m , and R_{ad} remains constant in this regime, whereas a reduction in the mean particle contact force f_w^m causes R_{ab} to decrease as R_{ab} is proportional to $f_w^{m3/2}$ as ($R_{ab} \propto n_a f_w^{m3/2}$).

The saturation of the MRR with increasing particle concentration has been observed experimentally. Biemann et al.³³ conducted W-CMP experiments using alumina particles with different particle sizes ($145 \text{ nm} \leq \mu_p \leq 1000 \text{ nm}$) and concentrations ($2\% \leq \eta_w \leq 15\%$). Experiments were performed with a hard pad (IC1000) under an applied pressure of $P_o = 0.045$ MPa (or $P_o = 6$ psi). In Fig. 14, we plot the MRR determined in these experiments. The MRR was normalized with respect to the largest measured MRR and plotted as a function of particle concentration η_w for different particle radii μ_p . The experimental conditions were simulated by our model using applied pressure, $P_o = 0.045$ MPa, pad elastic modulus, $E_s = 100$ MPa, and elastic modulus ratio, $E_s/E_p = 4$. The base parameters listed in Table I were used in the simulations. Figure 14 shows that the model using adhesive wear assumption accurately predicted the experimentally observed saturation effect for small particles ($\mu_p \leq 300$ nm). The experimentally observed saturation effect takes place for small particles, somewhere in the range of $5 < \eta_w^c < 10\%$ (Fig. 14), while the model predicts the critical particle concentration to be $\eta_w^c \approx 6.5\%$. The decrease in MRR above saturation particle concentration η_w^c predicted by the abrasive wear model was not seen in experiments. The saturation effect was not observed for large particles in the experiments ($\mu_p > 300$ nm). The model prediction for the critical particle concentration η_w^c does not depend on the particle size.

Forsberg⁷ reported CMP experiments on a silicon [Si(100)] wafer using silica slurry and a soft pad (Suba500). The applied pressure was adjusted to be $P_o = 0.009$ MPa ($P_o = 1.3$ psi), while the par-

tle concentration was varied in the range of $0 < \eta_w < 6.5\%$. The results of this experimental work are compared to the predictions of our model, with $E_s = 10$ MPa (for a soft pad), $E_s/E_p = 4$, and applied pressure $P_o = 0.009$ MPa. Other parameters of the model are listed in Table I. Figure 15 shows the comparison of normalized MRR found in the experiments and predicted by the simulations using adhesive and abrasive wear assumptions. The original data from the experiments are also shown in Fig. 15. Material removal is achieved in the experiments even when the particle concentration is reduced to 0, i.e., $\text{MRR} \sim 50$ nm/min for $\eta_w = 0\%$. This is attributed to the etching of the wafer material by slurry chemicals. To quantify the effect of particle concentration considering mechanical removal, MRR due to etching at $\eta_w = 0\%$ was subtracted from the experimental MRR, and then MRR was normalized with respect to the maximum MRR. Comparing the normalized MRR determined in the experiments and model results, good agreement was found for both adhesive and abrasive wear assumptions, except that the slight decrease in MRR for abrasive wear above saturation particle concentration η_w^c was not seen in experiments. The saturation particle concentration predicted by our model is $\eta_w^c \approx 6.5\%$ for adhesive wear, which is very similar to η_w^c predicted by the models for a hard pad $E_s = 100$ MPa and higher applied pressure $P_o = 0.045$ MPa given for a comparison with experiments by Biemann et al.³³ (Fig. 14). The effect of a softer pad is to increase the saturation concentration η_w^c , while a smaller particle material density ρ_p causes a

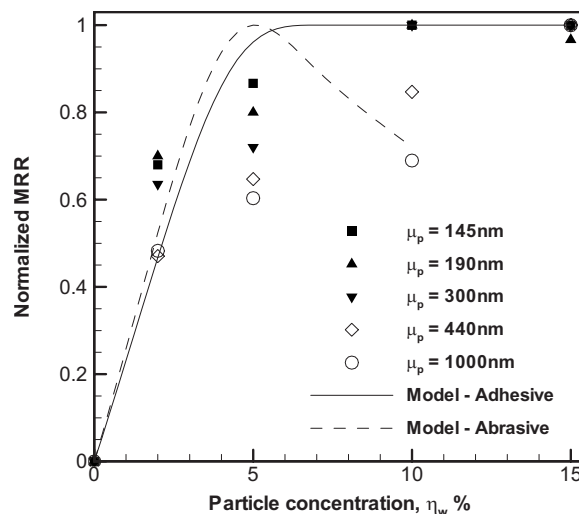


Figure 14. The comparison of the variation in normalized MRR with particle concentration η_w determined in experiments by Biemann et al.³³ and models.

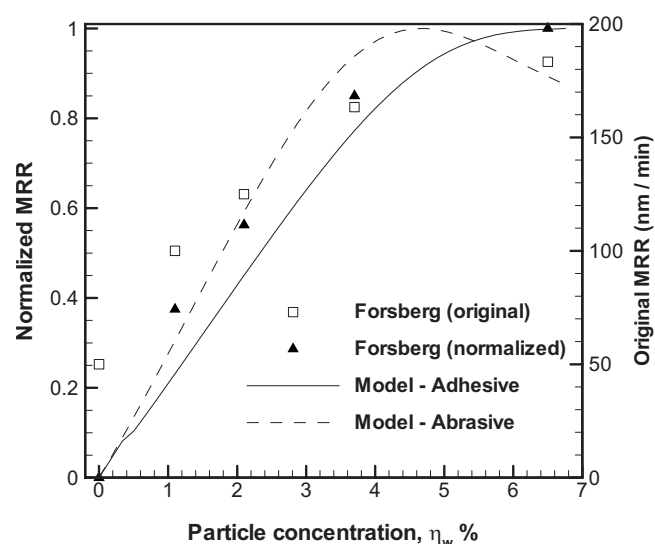
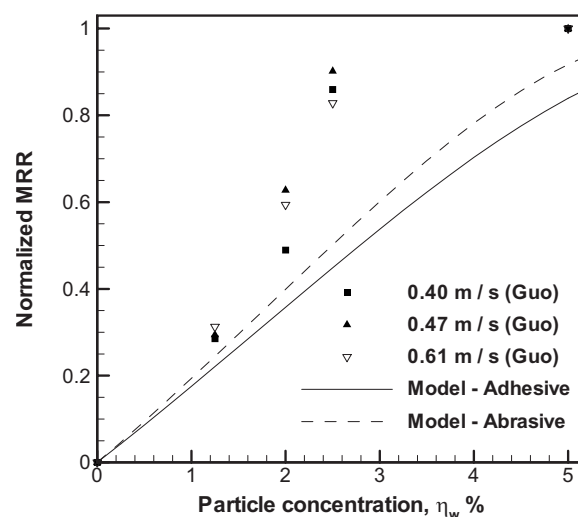


Figure 15. The comparison of the variation in normalized MRR with particle concentration η_w determined in experiments by Forsberg⁷ and models.

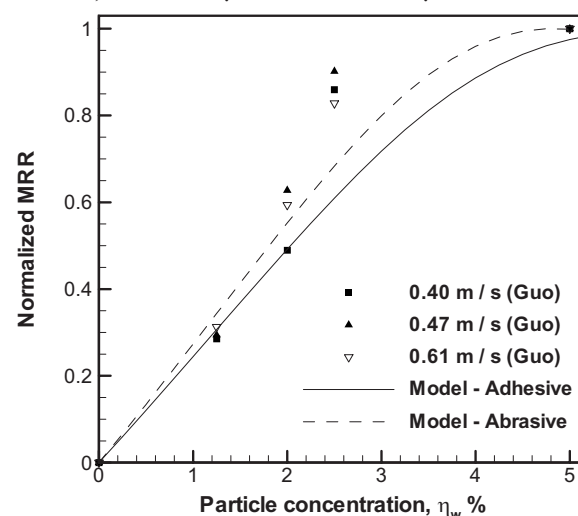
decrease in η_w^c . The material density of silica particles ($\rho_{si} = 2.5 \text{ g/cm}^3$) is smaller as compared to alumina particles ($\rho_{al} = 3.7 \text{ g/cm}^3$), which gives more particle volume for a given particle weight concentration η_w of silica particles. These two opposing effects offset each other, and the model predicts similar saturation particle concentration η_w^c values as observed in these separate experiments.

The variation in MRR as a function of particle concentration η_w was also studied experimentally for CMP of copper films with alumina slurry by Guo and Subramanian.⁹ In these experiments, CMP was performed with a hard pad (IC1000) and applied pressure was fixed at $P_o = 0.048 \text{ MPa}$ ($P_o = 6.8 \text{ psi}$), while three different relative velocities V_r were used. The results of these experiments were compared to our model, where simulations were carried out with the following pad elastic properties $E_s = 100 \text{ MPa}$ and $E_s/E_p = 4$ and applied pressure $P_o = 0.048 \text{ MPa}$. The results are given in Fig. 16. In Fig. 16a, where the pad-asperity radius is taken as $R_s = 50 \text{ }\mu\text{m}$, the model overpredicts the saturation particle concentration. The deviation between experiment and model results decreased for an asperity radius of $R_s = 100 \text{ }\mu\text{m}$ used in the model ($\sigma_s = 5 \text{ }\mu\text{m}$), as shown in Fig. 16b. A larger pad-asperity radius R_s shifts the model results for the saturation particle concentration η_w^c to a lower level. A similar effect can be obtained by decreasing the SD of pad roughness σ_s , which also causes the mean contact pressure P_m to decrease, as a smaller number of particles, n_a , are sufficient to prevent direct contact at lower local contact pressures. Good agreement was found between experiment and model results when $\sigma_s = 3 \text{ }\mu\text{m}$ is used in the model, as shown in Fig. 16c. Considering the effect of pad conditioning parameters on pad topography, it is possible that pad-asperity radius R_s and pad-asperity SD σ_s were different in experiments by Guo and Subramanian⁹ than the default values used in the model (Table I). The values in literature reflect this variation for different conditioning methods as pad-asperity radius in the range of $30 \text{ }\mu\text{m} \leq R_s \leq 100 \text{ }\mu\text{m}$ ^{17,34} and pad-asperity SD in the range of $3 \text{ }\mu\text{m} \leq \sigma_s \leq 29 \text{ }\mu\text{m}$ ^{35,36} were reported. Therefore, the model results are considered to be accurate although some adjustments for asperity radius R_s and SD σ_s within the ranges given in literature are required to match experimental results more closely.

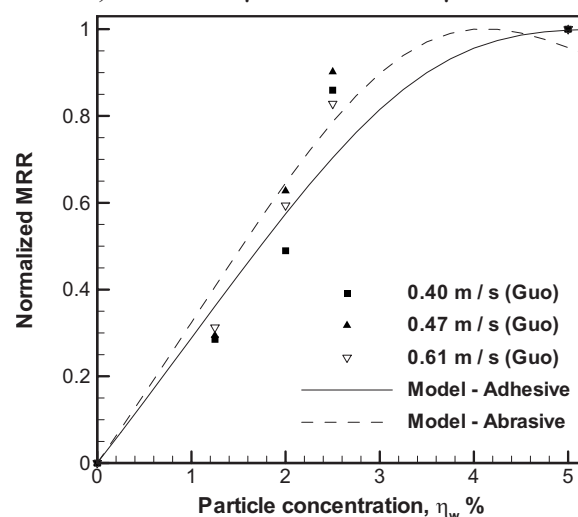
Effect of pad topography.— Although the applied pressure P_o is one of the important process parameters in CMP, the real contact pressure acting at the interface of the pad asperity and the wafer determines the characteristics of material removal. The surface to-



a) $R_s = 50 \text{ }\mu\text{m}$ and $\sigma_s = 5 \text{ }\mu\text{m}$



b) $R_s = 100 \text{ }\mu\text{m}$ and $\sigma_s = 5 \text{ }\mu\text{m}$



c) $R_s = 100 \text{ }\mu\text{m}$ and $\sigma_s = 3 \text{ }\mu\text{m}$

Figure 16. The comparison of the variation in normalized MRR with particle concentration η_w determined in experiments by Guo and Subramanian⁹ and models with asperity radius and pad roughness values of (a) $R_s = 50 \text{ }\mu\text{m}$ and $\sigma_s = 5 \text{ }\mu\text{m}$, (b) $R_s = 100 \text{ }\mu\text{m}$ and $\sigma_s = 5 \text{ }\mu\text{m}$, and (c) $R_s = 100 \text{ }\mu\text{m}$ and $\sigma_s = 3 \text{ }\mu\text{m}$.

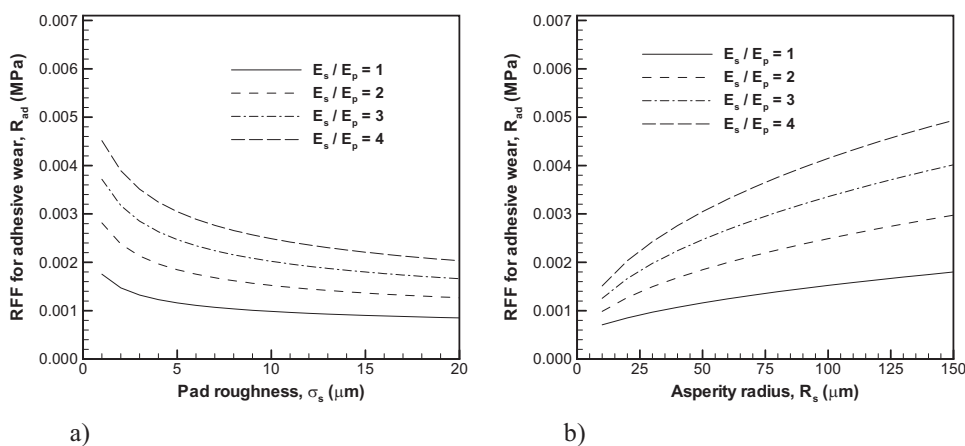


Figure 17. The effect of (a) pad roughness σ_s and asperity radius R_s on RFF due to adhesive wear R_{ad} for a soft pad $E_s = 10$ MPa with different porous elastic modulus ratios E_s/E_p .

pography of a rough pad influences the contact and the distribution of the applied pressure through the asperities on the wafer, and the mean real contact pressure P_m on each asperity and the real contact area A_r are, therefore, strong functions of pad topography. The mean pad-asperity radius R_s , the SD σ_s , the PDF Φ_s of the pad-asperity peak heights, and the areal density of asperity peaks are the parameters related to pad topography analyzed. A Gaussian distribution for PDF of asperity summit heights is employed in this work.

The mean contact pressure P_m and the real contact area A_r are related as $P_m = P_o/A_r$, where P_m decreases as contact spreads over a larger area. The real contact area A_r is the main controlling parameter for the number of active particles n_a , whereas the direct contact area A_d is a strong function of the mean contact pressure P_m . The general trends seen for the variation of RFF with pad topography are similar for a soft ($E_s = 10$ MPa) or hard ($E_s = 100$ MPa) pad and a low ($P_o = 0.007$ MPa) or high ($P_o = 0.07$ MPa) applied pressure. Furthermore, the effects of RFF due to adhesive wear R_{ad} are similar to that of abrasive wear R_{ab} . Therefore, in Fig. 17a and b, the variation in RFF due to adhesive wear R_{ad} is presented. The effects of the SD of pad-asperity summits σ_s and the mean pad-asperity radius R_s are investigated for $E_s = 10$ MPa and $P_o = 0.007$ MPa. These figures show that the RFF is higher for smaller σ_s or larger R_s values. This effect becomes more significant with increasing pad porosity E_s/E_p . This behavior can be explained as follows.

As the SD σ_s of the pad-asperity summits decreases, the real contact area A_r due to the pad-to-wafer contact increases, causing a mean contact pressure P_m to decrease (Fig. 18a). A lower mean contact pressure P_m decreases the tendency of particles to become embedded in the pad, thus diminishing the direct contact area ratio A_d/A_r , as demonstrated in Fig. 18b. This improves the ability of the pad to transfer applied pressure on the particles. These effects gen-

erally cause RFF to increase with smaller values of the SD σ_s of the pad roughness. Figure 18b also shows that the direct contact area ratio A_d/A_r does not vary significantly when porosity is small, e.g., $E_s/E_p = 1$, as direct contact remains dominant for different σ_s values. For more porous pads, e.g., $E_s/E_p = 4$, the mean contact pressure P_m transitions, with σ_s , from a particle-dominant to a direct-contact-dominant regime, where a small change in contact pressure translates to a significant variation in direct contact area A_d/A_r and particle contact pressure ratio P_p/P_o magnifying the effect of σ_s for large E_s/E_p . A similar mechanism explains the variation in RFF with respect to asperity radius R_s .

The effect of pad topography was investigated experimentally by performing oxide CMP experiments with silica slurry.³⁵ Two different conditioning disks, random diamond disk (RDD) and uniform diamond disk (UDD), were used to generate different pad topographies. RDD had diamonds with different distributed protrusion heights and shapes, while the protrusions on UDD were of pyramidal shape and had the same heights. As a result of the geometry of conditioning disks, pads conditioned by RDD had an SD of pad-asperity heights $\sigma_s = 4.94$ μm and skewness $S_s = 0.19$, whereas for pads conditioned by UDD these values were $\sigma_s = 2.96$ μm and $S_s = 0.44$, respectively. CMP experiments were performed by using each pad with an applied pressure, $P_o = 0.035$ MPa (=5 psi). The average MRR achieved using an RDD conditioned pad (320 nm/min) was 10% lower than the MRR achieved using a UDD conditioned pad (355 nm/min). We modeled the conditions of these experiments by introducing σ_s of each pad and by using $E_s = 100$ MPa, $E_s/E_p = 4$, with the base parameters listed in Table I. The effects of skewness were neglected. The model predicted the MRR of the RDD conditioned pad to be 14% lower than that of the UDD conditioned pad, which agrees with experiments.

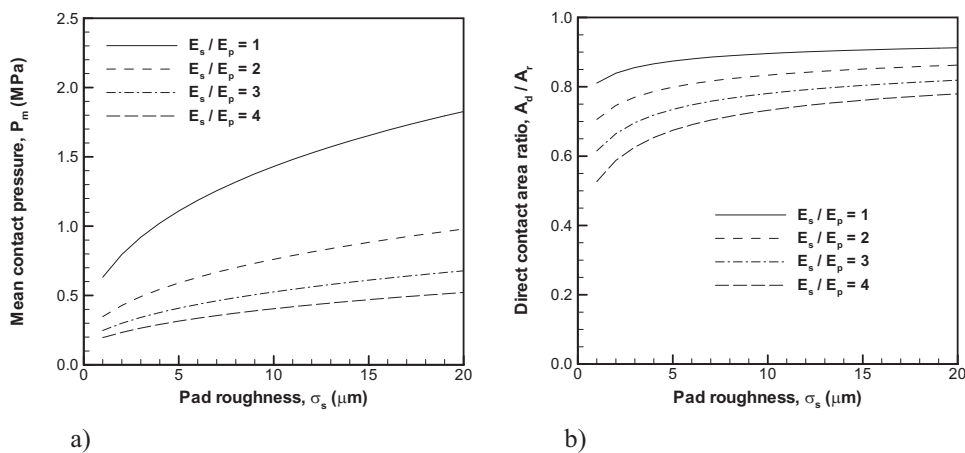


Figure 18. The effect of pad roughness σ_s on (a) real contact area ratio A_r and (b) mean contact pressure P_m for a soft pad $E_s = 10$ MPa with different porous elastic modulus ratios E_s/E_p .

Effect of passivated surface layer.—The slurry chemicals react with the wafer surface and form a passivated surface layer on the wafer. The hardness of this layer H_{pw} may be lower or higher than the hardness of the bulk wafer material H_{bw} .³⁷ The effective hardness H_w of the wafer is calculated based on Eq. 23. The indentation depth of a SP δ_w can be calculated as $\delta_w = f_w / (\pi r_p H_w)$ by using Eq. 22. Considering the dependence of the pad-to-particle contact force on the particle radius, f_p^p or $m \propto r_p^2$ (Eq. 3 and 4), the indentation depth is linearly proportional to the particle size (i.e., $\delta_w \propto r_p$). As the particle size r_p increases, the indentation depth of a particle δ_w becomes larger. If the passivated layer is softer than the bulk, this causes the effective hardness H_w to increase, or if the passivated layer is harder than the bulk, the effective hardness H_w decreases. This, in turn, has an effect on the MRR, as $RR_{ad} \propto 1/H_w$ and $RR_{ab} \propto 1/H_w^{3/2}$.

The effect of the mean abrasive particle size μ_p is investigated for different passivated layer thicknesses in the range of $0 < t_{pw} < 16$ nm, and $P_o = 0.007$ MPa (1 psi) in Fig. 19. The elastic modulus of a hard pad, $E_s = 100$ MPa, passivated layer hardness, $H_{pw} = 1000$ MPa, and bulk wafer hardness, $H_{bw} = 4000$ MPa, are used in this figure, along with the base values listed in Table I. Figure 19a shows that the mean indentation depth of particles δ_w^m increases linearly with mean particle radius μ_p when the passivated layer thickness t_{pw} is very small ($t_{pw} \sim 0$) or very large ($t_{pw} \sim 16$ nm). For intermediate values, e.g., $t_{pw} \sim 4$ or 8 nm, a change in slope occurs as the mean particle size μ_p exceeds a critical value, at which the particles start to indent through the passivated layer. As a result, effective hardness H_w increases with mean particle size μ_p , as shown in Fig. 19b, and approaches the bulk wafer hardness $H_w \sim H_{bw}$. A larger effective hardness H_w translates to a lower MRR as quantified by RFF normalized by effective wafer hardness, R_{ad}/H_w , plotted in Fig. 19c. An opposite behavior would be observed if the passivated wafer is harder than the bulk, $H_{pw} > H_{bw}$. In this case, MRR would decrease with a larger particle size μ_p for intermediate values of passivated layer thickness t_{pw} .²² The experimental findings in literature show both increasing^{38,39} and decreasing³³ trends for MRR with a larger particle size. The results presented here can help guide the interpretation of similar findings.

Conclusions

In this work, contact of a rough deformable pad and a smooth wafer with interfacial abrasive particles was analyzed. The interactions due to the two-body contact between the pad and the wafer (direct contact) and the three-body contact between the pad, the abrasive particles, and the wafer (particle contact) were considered. The model is extended for the computation of MRR for CMP by considering abrasive and adhesive wear mechanisms. The effects of these parameters are investigated, and the model results are compared with published experimental data. The results of this parametric analysis are summarized as follows.

1. Applied pressure: The model shows that the MRR has a power law relationship with applied pressure P_o . The power law exponent was computed to be in the range of $0.85 < n < 1.1$. The sublinear behavior corresponds to a soft pad (e.g., $E_s = 10$ MPa) with high porosity (e.g., $E_s/E_p = 4$). The value of n decreased with decreasing particle concentration η_w and a SD of pad roughness σ_s .
2. Pad substrate modulus and porosity: The model showed that stiffer pads (large E_s) and increased porosity cause the MRR to increase for both adhesive and abrasive wear assumptions.
3. Particle concentration: The model shows that the MRR increases linearly with the particle concentration η_w when η_w is small. A saturation effect was observed at a critical saturation particle concentration η_w^c , above which the MRR due to adhesive wear remains constant. For $\eta_w > \eta_w^c$, the MRR due to abrasive wear was predicted to decrease.
4. Pad roughness: The model results indicate that the MRR increases with a smaller SD of pad summits σ_s , whereas a larger

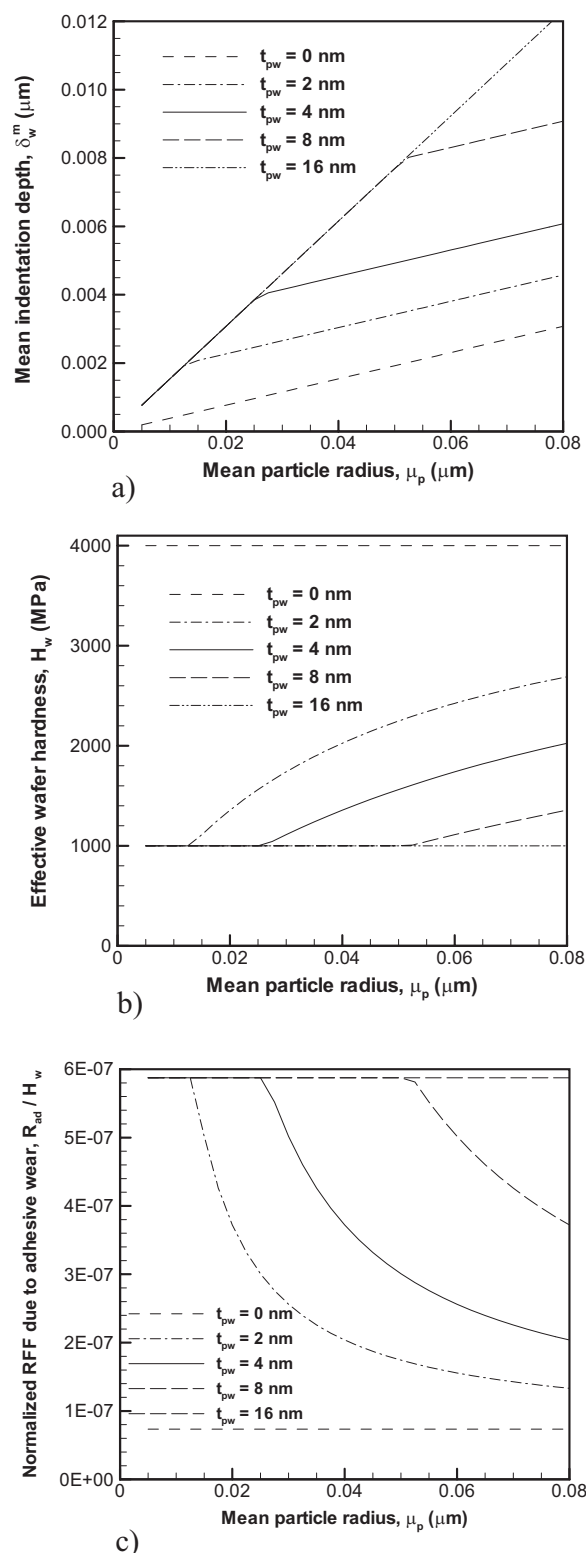


Figure 19. The effect of mean particle radius μ_p on (a) effective wafer hardness H_w and (b) MRR due to adhesive wear R_{ad} normalized with respect to effective wafer hardness for different passivated layer thicknesses t_{pw} ($H_{bw} = 4000$ MPa and $H_{pw} = 1000$ MPa).

summit radius R_s and an increased asperity density η_s causes the MRR to decrease.

5. Wafer hardness: The MRR becomes a function of particle size μ_p due to the effect of μ_p on the effective hardness. In the soft

passivated surface layer, a larger particle size μ_p results in lower MRR, while the opposite is true in the hard passivated surface layer.

6. Wear mechanism: A better agreement is found between the MRR predicted by the model using adhesive wear and experiments as compared to abrasive wear. Therefore, adhesive wear mechanism assumption seems to be more appropriate for CMP.

This work showed that the fraction of the applied pressure carried by particle contacts is an important factor affecting the MRR, as most of the materials are removed by the abrasive particles trapped between the pad asperities and the wafer. Each of the problem parameters, whose effects are summarized above, affects this fraction differently. Nevertheless, a contact mechanics approach was shown to be helpful in explaining the experimentally obtained trends. The authors hope that this and similar models can be used to design controlled experiments to investigate the complex interrelations between the various parameters that control material removal in CMP.

Acknowledgments

The authors thank H. C. Starck Incorporated for partial support of D.B.'s Ph.D. studies.

Northeastern University assisted in meeting the publication costs of this article.

References

1. *Chemical Mechanical Planarization of Semiconductor Materials*, M. R. Oliver, Editor, Springer, New York (2004).
2. G. Fu, A. Chandra, S. Guha, and G. Subhash, *IEEE Trans. Semicond. Manuf.*, **14**, 406 (2001).
3. F. W. Preston, *J. Soc. Glass Technol.*, **11**, 214 (1927).
4. V. H. Nguyen, R. Daamen, H. van Kranenburg, P. van der Velden, and P. H. Woerlee, *J. Electrochem. Soc.*, **150**, G689 (2003).
5. A. J. Clark, K. B. Witt, and R. L. Rhoades, in *Fourth CMP-MIC Conference*, Institute of Microelectronics On-Chip Interconnection, Santa Clara, CA, pp. 401–404 (1999).
6. J. Hernandez, P. Wrschka, Y. Hsu, T. S. Kuan, G. S. Oehrlein, H. J. Sun, D. A. Hansen, J. King, and M. A. Fury, *J. Electrochem. Soc.*, **146**, 4647 (1999).
7. M. Forsberg, *Microelectron. Eng.*, **77**, 319 (2005).
8. N. Chandrasekaran, S. Ramarajan, and W. Lee, *J. Electrochem. Soc.*, **151**, G882 (2004).
9. L. Guo and R. S. Subramanian, *J. Electrochem. Soc.*, **151**, G104 (2004).
10. P. Wrschka, J. Hernandez, Y. Hsu, T. S. Kuan, G. S. Oehrlein, H. J. Sun, D. A. Hansen, J. King, and M. A. Fury, *J. Electrochem. Soc.*, **146**, 2689 (1999).
11. D. Bozkaya and S. Müftü, *J. Tribol.*, **130**, 041401 (2008).
12. J. Luo and D. A. Dornfeld, *IEEE Trans. Semicond. Manuf.*, **14**, 112 (2001).
13. K. Qin, B. Moudgil, and C. W. Park, *Thin Solid Films*, **446**, 277 (2004).
14. G. Ahmadi and X. Xia, *J. Electrochem. Soc.*, **148**, G99 (2001).
15. J. A. Levert, Ph.D. Thesis, Georgia Institute of Technology, Atlanta, GA (1997).
16. J. A. Levert, F. M. Mess, R. F. Salant, and S. Danyluk, *Tribol. Trans.*, **41**, 593 (1998).
17. L. Shan, J. Levert, L. Meade, J. Tichy, and S. Danyluk, *J. Tribol.*, **122**, 539 (2000).
18. J. Tichy, J. A. Levert, L. Shan, and S. Danyluk, *J. Electrochem. Soc.*, **146**, 1523 (1999).
19. J. Lu, C. Rogers, V. P. Manno, A. Philipossian, S. Anjur, and M. Moinpour, *J. Electrochem. Soc.*, **151**, G241 (2004).
20. L. J. Borucki, T. Sun, Y. Zhuang, D. Slutz, and A. Philipossian, in *Proceedings of the MRS Spring Conference 2009*, Materials Research Society, Paper no. 1157-E01-02 (2009).
21. L. J. Gibson and M. F. Ashby, *Cellular Solids: Structure and Properties*, Cambridge University Press, New York (1997).
22. D. Bozkaya, Ph.D. Thesis, Northeastern University, Boston, MA (2009).
23. A. T. Kim, J. Seok, J. A. Tichy, and T. S. Cale, *J. Electrochem. Soc.*, **150**, G570 (2003).
24. E. Rabinowicz, *Friction and Wear of Materials*, John Wiley & Sons, New York (1995).
25. M. Bastaninejad and G. Ahmadi, *J. Electrochem. Soc.*, **152**, G720 (2005).
26. R. Saxena, D. G. Thakurta, R. J. Gutmann, and W. N. Gill, *Thin Solid Films*, **449**, 192 (2004).
27. D. G. Thakurta, C. L. Borst, D. W. Schwendeman, R. J. Gutmann, and W. N. Gill, *J. Electrochem. Soc.*, **148**, G207 (2001).
28. H. Hertz, *J. Reine Angew. Math.*, **92**, 156 (1882).
29. J. A. Greenwood and J. B. P. Williamson, *Proc. R. Soc. London, Ser. A*, **295**, 300 (1966).
30. Y. Moon, I. Park, and D. A. Dornfeld, in *ASPE 1998 Spring Topical Meeting on Silicon Machining*, Monterey, CA, Vol. 17, pp. 78–82 (1998).
31. Y. Moon, I. Park, and D. A. Dornfeld, in *ASPE 1998 Spring Topical Meeting on Silicon Machining*, Monterey, CA, Vol. 17, pp. 83–87 (1998).
32. M. Fury and D. James, in *SPIE Microelectronic Manufacturing Symposium*, Austin, TX (1996).
33. M. Bielmann, U. Mahajan, and R. K. Singh, *Electrochem. Solid-State Lett.*, **2**, 401 (1999).
34. T. Yu, C. C. Yu, and M. Orlowski, *Tech. Dig. - Int. Electron Devices Meet.*, **1993**, 865.
35. K. Park and H. Jeong, *J. Electrochem. Soc.*, **155**, H595 (2008).
36. D. Stein, D. Hetherington, M. Dugger, and T. Stout, *J. Electron. Mater.*, **25**, 1623 (1996).
37. R. Ihnfeldt and J. B. Talbot, *J. Electrochem. Soc.*, **155**, H412 (2008).
38. D. Tamboli, G. Banerjee, and M. Waddell, *Electrochem. Solid-State Lett.*, **7**, F62 (2004).
39. J. Y. Lai, Ph.D. Thesis, Massachusetts Institute of Technology, MA (2001).